Petroleum Science 23 (2026) 3892–3905

Contents lists available at ScienceDirect

Petroleum Science

journal homepage: www.keaipublishing.com/en/journals/petroleum-science

Original Paper

Closed-loop porosity inversion method with well-seismic joint constraints based on wavelet transform

Teng-Fei Chen [a,b], Guang-Zhi Zhang [a,b,*], Hong-Jian Hao [a,b], De-Kuan Chang [c], Jian-Hu Gao [c], Gang Gao [d]

[a] State Key Laboratory of Deep Oil and Gas, China University of Petroleum (East China), Qingdao, 266580, Shandong, China
[b] School of Geosciences, China University of Petroleum (East China), Qingdao, 266580, Shandong, China
[c] Research Institute of Petroleum Exploration and Development NorthWest, PetroChina, Lanzhou, 730020, Gansu, China
[d] Key Laboratory of Exploration Technologies for Oil and Gas Resources (Yangtze University), Ministry of Education, Wuhan, 430100, Hubei, China

A R T I C L E I N F O

Article history:
Received 26 September 2025
Received in revised form
5 January 2026
Accepted 10 March 2026
Available online 20 March 2026

Edited by Meng-Jiao Zhou

Keywords:
Porosity inversion
Kernel density estimation
Wavelet transform
Closed-loop neural network
Constraints of seismic and well logging

A B S T R A C T

Porosity is one of the key physical properties of reservoir rocks, directly influencing their capacity to store and transmit oil and gas. Traditional porosity inversion methods are often constrained by the resolution of seismic data, lateral continuity, and secondary inversion errors, which hinder their ability to characterize reservoir properties in complex geological settings. Therefore, a closed-loop porosity inversion method with well-seismic joint constraints based on wavelet transform is proposed to predict porosity directly from post-stack seismic data. This method amplifies the training samples using kernel density estimation, thereby alleviating network instability and overfitting caused by insufficient training data. Subsequently, the seismic data is divided into low-, medium-, and high-frequency information using the wavelet transform, and the local spatial features of different scales are extracted using convolution kernels of different sizes. At the same time, the temporal features of full-frequency post-stack seismic data are extracted using gated recurrent units. Then, a forward network is constructed to replace the implicit convolution model between the post-stack seismic data and porosity, thereby establishing a closed-loop mapping from the post-stack seismic data to full-frequency porosity and back to the post-stack seismic data. Finally, the test results on the thin-layer alternating geological model and actual data show that the method proposed improves the lateral continuity of the inversion results while maintaining the vertical resolution.

1. Introduction

Porosity is an important physical parameter of formation rock, which directly affects the fluid storage capacity and fluidity of the reservoir. Currently, there are two primary methods for porosity prediction: (i) laboratory core analysis, and (ii) well logging or joint well-seismic inversion. Given the high cost of laboratory core analysis and the discontinuity of coring (Yang et al., 2024), although the evaluation results of the first method are more accurate, it is less commonly applied in practice. Therefore, the latter method is the most commonly used in reservoir parameter prediction. Previously, porosity was typically calculated quantitatively using a linear equation derived from the combination of three porosity logs (Khaksar and Griffiths, 1998). The porosity of clean sandstone formations was estimated using sonic transit-time data from well logs in combination with the classical Wyllie–Clemenceau equation (Kamel et al., 2002). A correction method for estimating effective porosity was proposed by Abid et al. (2025), integrating density and neutron log data with numerical equations and being applicable to both conventional and unconventional reservoirs. However, due to the influence of various geological factors such as burial depth and depositional environment, this method cannot effectively extrapolate between wells. To address this, researchers have integrated logging data and seismic data, capitalizing on their complementary strengths in vertical and horizontal resolution, as well as three-dimensional spatial coverage, to predict the spatial distribution of reservoir parameters (Wang et al., 2019; Bashir et al., 2024; Zhang et al., 2025).

* Corresponding author.
E-mail address: zhanggz@upc.edu.cn (G.-Z. Zhang).

Peer review under the responsibility of China University of Petroleum (Beijing).

https://doi.org/10.1016/j.petsci.2026.03.020
1995-8226/

The reservoir parameters of well-seismic joint inversion can be divided into two categories: model-driven and data-driven methods. The model-driven methods usually rely on rock physics models and forward modeling, and gradually adjust model parameters to match observed data with seismic response constraints (Wyllie et al., 1956; Xu and Payne, 2009; Pan et al., 2017). For example, multiple poroelastic parameters were estimated by Barros et al. (2010) using Biot's poroelastic theory within a full-waveform inversion framework. A porosity prediction expression based on the Gassmann equation and the comprehensive rock skeleton model was derived by Liu et al. (2014), and the seismic inversion data were combined to predict the three-dimensional porosity. A joint estimation method for rock physical properties that combines statistical rock physics with Bayesian seismic inversion to capture the complexity of reservoir characteristics was proposed by Figueiredo et al. (2018). A Bayesian probabilistic seismic inversion method that estimates the posterior probability distribution via the expectation maximization algorithm was proposed by Pan et al. (2018). However, the accuracy of the above methods depends on the accurate calculation of geophysical parameters, some of which are often difficult to obtain, thus increasing the complexity and uncertainty of the model. Moreover, the simplified assumptions in rock physics models may fail to capture the heterogeneity and complex pore structures of reservoirs realistically, and these methods are also sensitive to the choice of initial parameters and prior assumptions, which can lead to biased or unstable inversion results in areas with sparse well control or highly variable geology. These factors collectively limit the applicability and robustness of model-driven porosity prediction methods in complex geological environments.

The data-driven methods use the powerful data processing ability of neural networks to extract the features of data, and have achieved remarkable results in reservoir prediction, lithology identification, and seismic facies division (Zhang et al., 2022; Zhai et al., 2024; Wang et al., 2025; Das et al., 2019; Pan et al., 2024). A single-layer and a double-layer convolutional neural network were used by Duan et al. (2016) to construct a mapping between logging data and porosity. The temporal information of logging data was captured using a gated recurrent unit (GRU) by Sun and Liu (2020) for curve prediction. Although the above methods have achieved good results, the use of neural networks for reservoir parameter inversion has the problem of insufficient training samples, resulting in unstable inversion results. To overcome these challenges, some scholars use network fusion or add prior information for inversion (Liu et al., 2022; Chen et al., 2023; Zhang et al., 2022; Han et al., 2022; Sang et al., 2024). A method that fuses recurrent neural networks (RNNs) and convolutional neural networks (CNNs) to extract low- and high-frequency information from seismic data for seismic impedance inversion was proposed by Alfarraj and AlRegib (2019). A closed-loop CNN network that performs inversion and forward modeling of unlabeled seismic data to alleviate the problem of insufficient training samples was proposed by Wang et al. (2020). A closed-loop seismic inversion method based on CNN and geostatistics was proposed by Ge et al. (2022) to achieve high-resolution impedance inversion for thinly interbedded reservoirs. In parallel, strategies that combine data-driven methods with traditional signal processing can also mitigate the instability of neural networks caused by insufficient training samples (Zhang et al., 2025; Tong et al., 2025; Zhang et al., 2025). For instance, wavelet transforms combined with neural networks have been successfully applied to enhance the feature representation of logging data for reservoir fluid identification by Gong and Zhang (2024). The combination of frequency decomposition and intelligent inversion was applied to three-dimensional facies modeling to improve the prediction accuracy of analogous reservoirs by Wang et al. (2024). Although the above methods can effectively alleviate the instability of inversion results caused by insufficient training of neural networks, insufficient training samples may still lead to the inability of neural networks to fully learn complex geological features. Therefore, some scholars use kernel density estimation (KDE) for sample amplification to improve the prediction effect of the network on sparse geological areas. A Gaussian KDE-based GK-SMOTE method was proposed by Miraj et al. (2025), in which synthetic samples are generated to enhance class separability and thereby address the class imbalance problem. New samples are amplified from the probability distribution of minority-class data based on kernel density estimation by Kamalov and Elnagar (2021), and the performance of neural networks in classification tasks is effectively improved. A virtual sample generation method based on UMAP-KDE was proposed by Mukun et al. (2024), in which sparse small-sample data are expanded through kernel density estimation, and the prediction performance and generalization ability of the soft-sensing model are effectively improved.

Given the effectiveness of kernel density estimation in sample augmentation, it is combined with neural networks and wavelet transform to propose a closed-loop porosity inversion method based on wavelet transform (WTCLPI), aiming to improve the generalization ability and stability of the model. The samples are decomposed into different frequency bands using a wavelet transform, and these bands are then combined with the full-frequency post-stack seismic data as inputs to the network, thereby enhancing the identification of thin interbeds and local anomalies. To better capture spatiotemporal dependencies, spatiotemporal attention mechanisms are integrated with 3D CNN and GRU modules. Furthermore, the forward model is replaced by a neural network, and a closed-loop mapping from the post-stack seismic data to full-frequency porosity and then back to the post-stack seismic data is established. Inversion experiments on both thin interbedded models and shale oil reservoirs demonstrated that the method proposed significantly improved the accuracy and lateral continuity of inversion results compared to traditional closed-loop approaches.

2. Method

2.1. Kernel density estimation

Kernel density estimation is a non-parametric probability density estimation method, which is used to estimate the probability density function of random variables through observation samples in the case of unknown data distribution. Suppose there is a set of independent and identically distributed samples $\mathbf{X} = \{x_1, x_2, \cdots, x_n\}$, and the density function of the real distribution is $f(x)$, then the KDE estimation expression is:

$$f(x) = \frac{1}{nh}\sum_{i=1}^{n} K\left(\frac{x - x_i}{h}\right) \tag{1}$$

where K is the Gaussian kernel function; h >0 is the bandwidth parameter, which determines the smoothness of the estimation results; n is the number of sampling points.

2.2. Wavelet transform

The wavelet transform is a time-frequency analysis method of signals. Its core idea is to use a set of wavelet functions with localized time and frequency features to decompose the signal and extract information of different scales. Assuming that the signal is $f(t)$, its wavelet transform can be expressed as:

$$f(t) = \sum_j \sum_k c_{j,k} \psi_{j,k}(t) \tag{2}$$

where $c_{j,k}$ is the wavelet coefficient, which represents the projection of the signal at different scales and positions. $\psi_{j,k}$ is the wavelet basis function, which is obtained by shifting k and scaling j, and is used to analyze the features of signals at different times and frequencies. The wavelet transform decomposes the signal into low-frequency and high-frequency information of multiple scales. By applying a series of low-pass and high-pass filters to the signal.

2.3. Convolutional neural network

The 3D convolutional neural networks extend 2D convolutional neural networks by performing convolutional operations across three dimensions, enabling the processing of data with both spatial and temporal dimensions. The 3D convolutional kernels convolve with the input data, allowing the model to capture more local features and complex spatial relationships.

$$Y(i,j,k) = \sum_{m=0}^{M-1} \sum_{n=0}^{N-1} \sum_{p=0}^{P-1} X(i+m, j+n, k+p) \cdot \mathbf{W}(m,n,p) \tag{3}$$

where $Y(i,j,k)$ is the output spatial feature. $X(i+m,j+n,k+p)$ is the input feature. $\mathbf{W}(m,n,p)$ is the weight of the 3D convolutional kernel at position (m,n,p). M, N, and P represent the size of the convolutional kernel in the depth (Z-axis), height (Y-axis), and width (X-axis) directions, respectively.

2.4. Gated recurrent unit

A gated recurrent unit is a type of recurrent neural network architecture designed to address the vanishing gradient problem commonly encountered in traditional RNNs (Bengio et al., 1994). The reset and update gates introduced by Cho et al. (2014) simplify the architecture compared to long short-term memory while maintaining strong performance in tasks such as sequence data analysis.

$$\mathbf{z}_t = \sigma(\mathbf{W}_z \cdot [\mathbf{h}_{t-1}, \mathbf{x}_t] + \mathbf{b}_z) \tag{4}$$

$$\mathbf{r}_t = \sigma(\mathbf{W}_r \cdot [\mathbf{h}_{t-1}, \mathbf{x}_t] + \mathbf{b}_r) \tag{5}$$

$$\tilde{\mathbf{h}}_t = \tanh(\mathbf{W}_h \cdot [\mathbf{r}_t \odot \mathbf{h}_{t-1}, \mathbf{x}_t] + \mathbf{b}_h) \tag{6}$$

$$\mathbf{h}_t = (1 - \mathbf{z}_t) \odot \mathbf{h}_{t-1} + \mathbf{z}_t \odot \tilde{\mathbf{h}}_{t-1} \tag{7}$$

where $\mathbf{W}_z$ and $\mathbf{W}_r$ are the weight matrices for the update gate and reset gate, $\mathbf{W}_h$ is the weight matrix for the candidate hidden state, $\mathbf{h}_{t-1}$ is the hidden state from the previous time step, $\mathbf{x}_t$ is the input at the current time step, the function σ represents the sigmoid activation function, $\odot$ denotes the element-wise multiplication of the reset gate with the previous hidden state.

2.5. Temporal attention mechanism

Although GRU uses reset and update gates to ensure the long-term dependence of data, it cannot adequately highlight the impact of critical temporal features on the output. Therefore, a temporal attention mechanism is integrated with GRU to allocate varying weight coefficients to different temporal features. The temporal features are assumed to be representable as $\mathbf{H}_n = [H_{1,n}, H_{2,n}, H_{3,n}, \cdots, H_{t,n}]$, where t denotes the length of the temporal sequence and n indicates the dimensionality.

$$\boldsymbol{\beta}'_n = softmax(\mathbf{W}_\beta \mathbf{H}_n + \mathbf{b}_\beta) \tag{8}$$

$$\mathbf{X}''_n = \boldsymbol{\beta}'_n \odot \mathbf{H}_n = \left[\beta_{1,n} H_{1,n}, \beta_{2,n} H_{2,n}, \cdots, \beta_{t,n} H_{t,n}\right] \tag{9}$$

where $\boldsymbol{\beta}'_n = [\beta_{1,n}, \beta_{2,n}, \beta_{3,n}, \cdots, \beta_{t,n}]$ are the weight coefficients. *softmax* is a normalized function. $\mathbf{W}_\beta$ and $\mathbf{b}_\beta$ are the weight matrix and bias, respectively. $\odot$ denotes the dot product between two vectors. $\mathbf{X}''_n$ is the final output.

2.6. Spatial attention mechanism

The correlation among various logging or seismic data differs, yet conventional models fail to emphasize the impact of critical spatial features on the target labels. To address this, a spatial attention mechanism is integrated into the CNN, enabling the assignment of distinct weight coefficients to different spatial features. The spatial features are assumed to be representable as $\mathbf{h}_t = [h_{t,1}, h_{t,2}, h_{t,3}, ..., h_{t,n}]$, where t denotes the t th convolution kernel and n indicates the number of channels in the kernel.

$$\boldsymbol{\alpha}'_t = softmax(\mathbf{W}_\alpha \mathbf{h}_t + \mathbf{b}_\alpha) \tag{10}$$

$$\mathbf{X}'_t = \boldsymbol{\alpha}'_t \odot \mathbf{h}_t = [\alpha_{t,1} h_{t,1}, \alpha_{t,2} h_{t,2}, \alpha_{t,3} h_{t,3}, \cdots, \alpha_{t,n} h_{t,n}] \tag{11}$$

where $\boldsymbol{\alpha}'_t = [\alpha_{t,1}, \alpha_{t,2}, \alpha_{t,3}, \cdots, \alpha_{t,n}]$ are the weight coefficients. $\mathbf{X}'_t$ is the final output result.

2.7. Forward network

Since seismic data can be regarded as the convolution of formation reflection coefficients and seismic wavelets, this process is highly similar to the convolution process in a 1D convolutional neural network. Therefore, a forward network consisting of two 1D CNNs and a fully connected layer is constructed (Fig. 1). The spatial features of porosity are extracted by the first 1D convolutional neural network, and the data features are convolved with the second 1D CNN and fitted through a fully connected layer. The L_2 norm is used to calculate the error between synthetic and real seismic data, and the forward network is trained using the back-propagation algorithm to adjust model parameters and optimize performance.

2.8. WTCLPI fusion network

The WTCLPI fusion network is composed of CNN, GRU, and a spatiotemporal attention mechanism (Fig. 2). The full-frequency post-stack seismic data and the low-, medium-, and high-frequency information obtained by wavelet transform are input into the GRU and the CNN, respectively, to extract the temporal and spatial features. Then, different weight coefficients are assigned to different spatiotemporal features through the spatio-temporal attention mechanism, allowing the network to focus more on important spatiotemporal features. Finally, a fully connected layer establishes the nonlinear relationship between post-stack seismic data and full-frequency porosity.

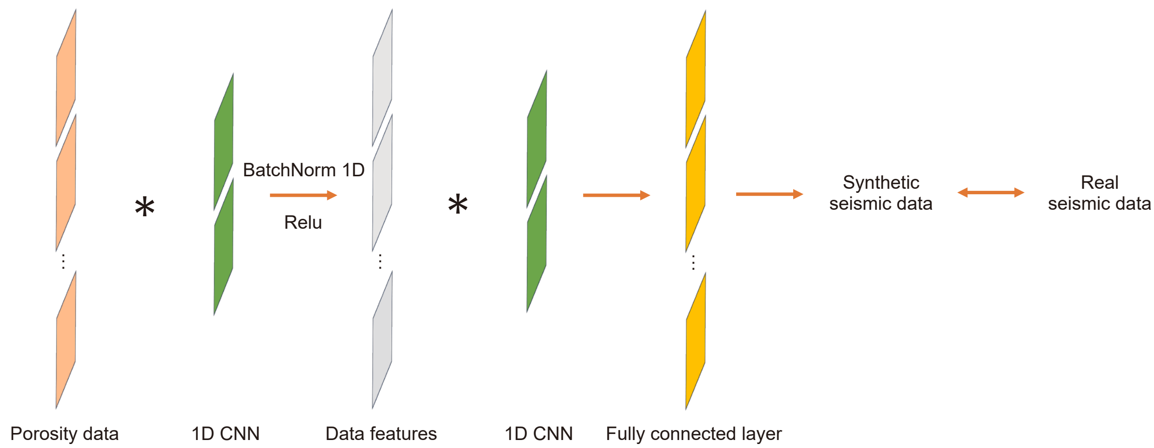

Fig. 1. Structure of the forward network.

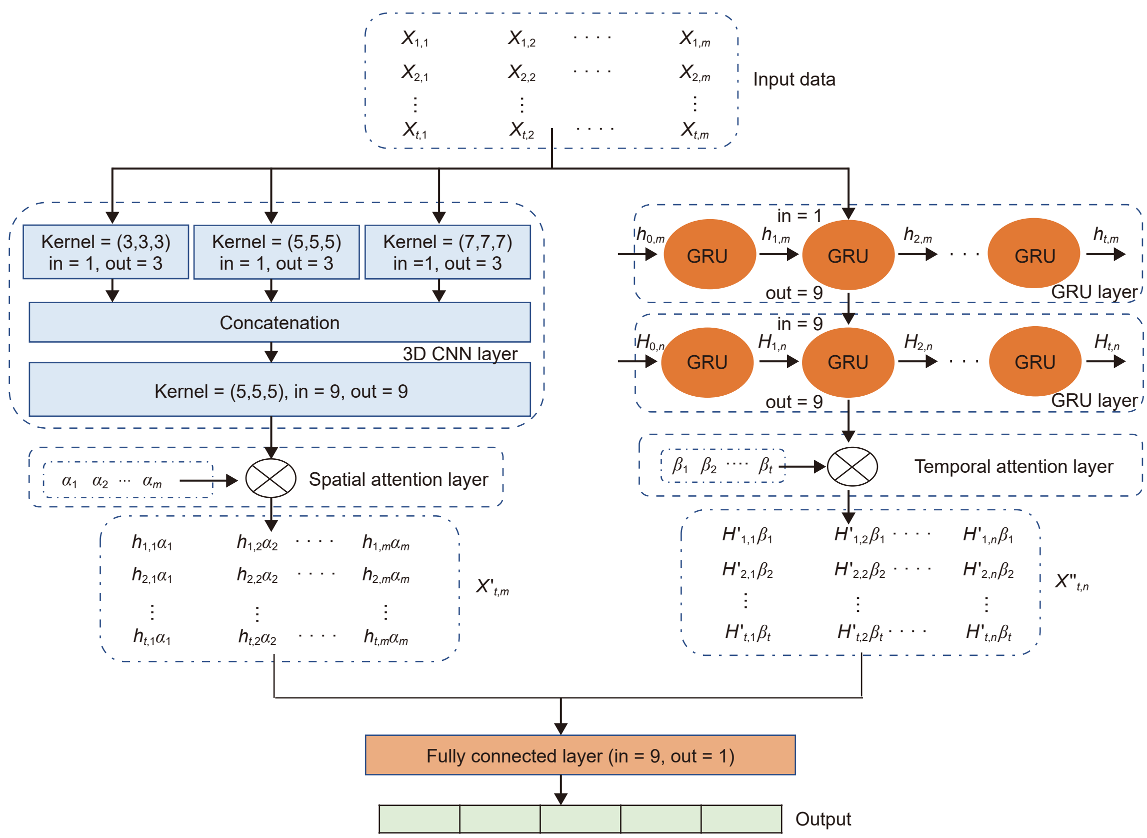

Fig. 2. Structure of the WTCLPI fusion network.

2.9. Prediction process of porosity inversion

The inversion process of the WTCLPI fusion network involves the following steps (Fig. 3):

(1) Dataset preparation: Normalization and standardization are applied to the post-stack seismic data and porosity to reduce dimensional discrepancies.

(2) Wavelet decomposition: The post-stack seismic data are decomposed by wavelet transform into low- ($S_{\_lowseis}$), medium- ($S_{\_midseis}$), and high-frequency ($S_{\_highseis}$) information, which are then combined with the full-frequency post-stack seismic data as input to the neural network.

(3) Loss function construction: Firstly, the inversion results of the WTCLPI fusion network (Y_{P_label}) are compared with the real values ($Y_{\_label}$) using the L_2 norm to obtain the error of the logging loss. Under the constraint of λ_1, the high-frequency information of the logging data is compensated into the post-stack seismic data to improve the vertical resolution of the inversion results. Secondly, the low-frequency information of the inversion results (Y_{P_filter}) is extracted using a low-pass filter and compared with the original low-frequency information ($Y_{\_filter}$) obtained from well-seismic joint interpolation. Under the constraint of λ_2, the low-frequency information of the inversion results is controlled. Thirdly, the unlabeled post-stack seismic data

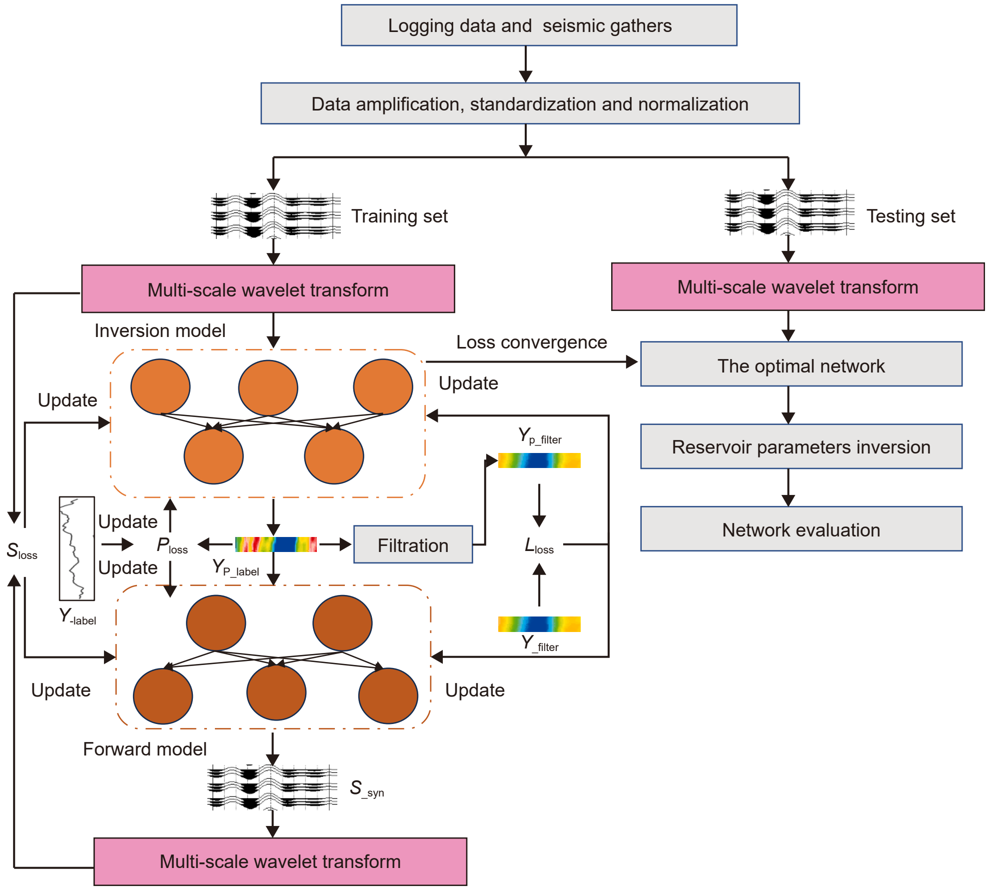

Fig. 3. The inversion process of the WTCLPI fusion network.

are included in the current cycle, and the unlabeled porosity prediction values ($Y_{P\_unlabel}$) are obtained using the WTCLPI fusion network. These predicted values are then input into the forward network to generate synthetic seismic data ($S_{\_syn}$), and the low- ($S_{\_lowsym}$), medium- ($S_{\_midsym}$), and high-frequency ($S_{\_highsym}$) information of the synthetic seismic data are obtained by wavelet transform, and the seismic loss of different frequency bands is calculated by L_2. This process indirectly ensures the stability of the porosity inversion results at non-well locations. Under the action of λ_3, the degree of lateral constraint on the inversion results is improved. By constructing the loss function, the network can be trained using a large number of unlabeled seismic data, thereby enhancing the generalization ability of the network and improving the stability of the inversion results.

$$\mathrm{Loss}=\frac{\lambda_1}{N}\sum_{i=1}^{N}\left|\left|Y_{\_label}-Y_{p\_label}\right|\right|_2^2+\frac{\lambda_2}{M}\sum_{i=1}^{M}\left|\left|Y_{P\_filter}-Y_{\_filter}\right|\right|_2^2+ \frac{\lambda_3}{M}\sum_{i=1}^{M}\left(\omega_1\left|\left|S_{\_lowsyn}-S_{\_lowseis}\right|\right|_2^2+\omega_2\left|\left|S_{\_midsyn}-S_{\_midseis}\right|\right|_2^2+\omega_3\left|\left|S_{\_highsyn}-S_{\_highseis}\right|\right|_2^2\right) \tag{12}$$

where M and N represent the number of seismic and logging data, respectively. The weight coefficients for both the model and the real data are set to $\lambda_1 = 0.5$, $\lambda_2 = 0.2$, and $\lambda_3 = 0.3$. ω_1, ω_2 and ω_3 represent the weight coefficients of different frequency bands, respectively. Due to the narrow effective bandwidth of seismic data, high-frequency information is more likely to be lost or attenuated than low-frequency and medium-frequency information during seismic inversion. To make up for this problem and improve the inversion accuracy, different weights are given to different frequency bands according to the experimental results. The weights of low-frequency, medium-frequency, and high-frequency are set to 1,1, and 1.4, respectively.

(4) Network evaluation: The essence of neural network inversion of reservoir parameters is to fit the data. Therefore, the root mean square error (RMSE) and the coefficient of determination (R^2), which are two evaluation metrics commonly used in regression analysis, are used to evaluate the effectiveness of the method. In addition, the lateral gradient evaluation index (LGE) is introduced to quantitatively evaluate the lateral variation characteristics. A lower LGE value indicates weaker lateral gradient variations and a more continuous overall lateral structure.

$$\mathrm{RMSE}=\sqrt{\frac{1}{m}\sum_{i=1}^{m}(y_i-\hat{y}_i)^2} \tag{13}$$

$$R^2=1-\frac{\sum_{i=1}^{m}(y_i-\hat{y}_i)^2}{\sum_{i=1}^{m}(y_i-\bar{y})^2} \tag{14}$$

$$\mathrm{LGE} = \frac{1}{(N_x-1)N_y}\sum_{j=1}^{N_y}\sum_{i=1}^{N_x-1}|p(i+1,j)-p(i,j)| \tag{15}$$

where y_i represents the real value, $\bar{y}$ represents the mean of the real value, $\hat{y}_i$ represents the predicted value, and m is the number of samples. $p(i,j)$ denotes the inversion result at the (i,j) position on the inverse slice, the number of N_x lateral traces, and the number of N_y longitudinal traces.

3. Inversion experiment

3.1. Introduction of model data

To evaluate the effectiveness of the method, a thin interbedded geological model (Fig. 4) is constructed, which includes 474 CDPs, 253 sampling points, and a sampling interval of 0.5 ms. The model consists of six shale layers (S1 to S6) with thicknesses ranging from 3 m to 5 m. Specifically, S4 represents a pinch-out area, whereas S5 and S6 correspond to a superimposed area. The model includes four wells: A, B, C, and D. Wells A, B, and D are amplified using KDE, generating 1000 additional samples, with a portion of these samples shown in Fig. 5, while well C is used as a verification well for network evaluation.

Fig. 6 shows the post-stack seismic data obtained by convolving the acoustic impedance calculated from compressional velocity and density based on DEM, KT, and Gassmann models with a 25 Hz Ricker wavelet (He et al., 2020; Zhang et al., 2021; Ba et al., 2023). It is observed that post-stack seismic data cannot effectively resolve the pinch-out (blue box) and superimposed areas (red box). Fig. 7 shows the information of different frequency bands of post-stack seismic data obtained by wavelet transform. Based on frequency bandwidth classification, the 0–10 Hz band represents low-frequency information, typically associated with large-scale geological features such as deep structures and regional tectonics. The 11–30 Hz band corresponds to medium-frequency information, capable of revealing certain geological heterogeneities, such as individual strata or localized changes. The above 30 Hz band represents high-frequency information, which are often used to detect fine-scale geological variations or small-scale structural details. To address the instability of neural network inversion results caused by limited training samples, the initial low-frequency information of porosity is obtained by well-seismic joint interpolation (Fig. 8), which is used as a priori information to constrain the inversion process.

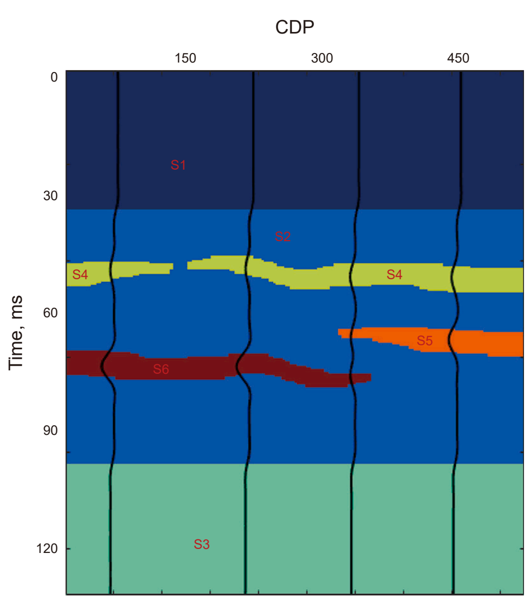

Fig. 4. Geological model of thin interbed.

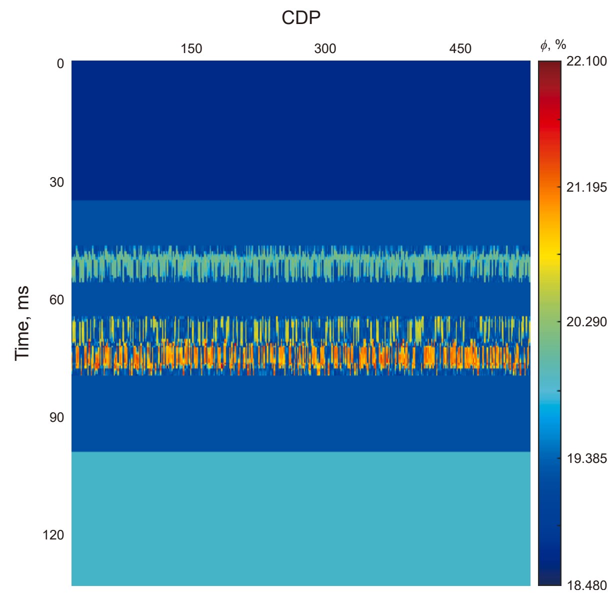

Fig. 5. Partial parameters generated randomly.

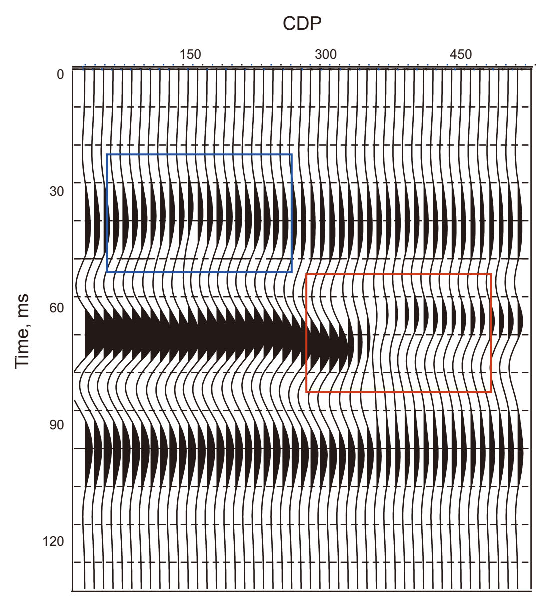

Fig. 6. Post-stack seismic data.

3.2. Model testing and analysis

To verify the effectiveness of the WTCLPI fusion network, its inversion results are compared with those of the traditional closed-loop neural network (Fig. 9(a)–(c)). It is observed that although the inversion results of the two methods on the training data are very good, the WTCLPI fusion network achieves better performance in identifying superimposed (black box) and pinch-

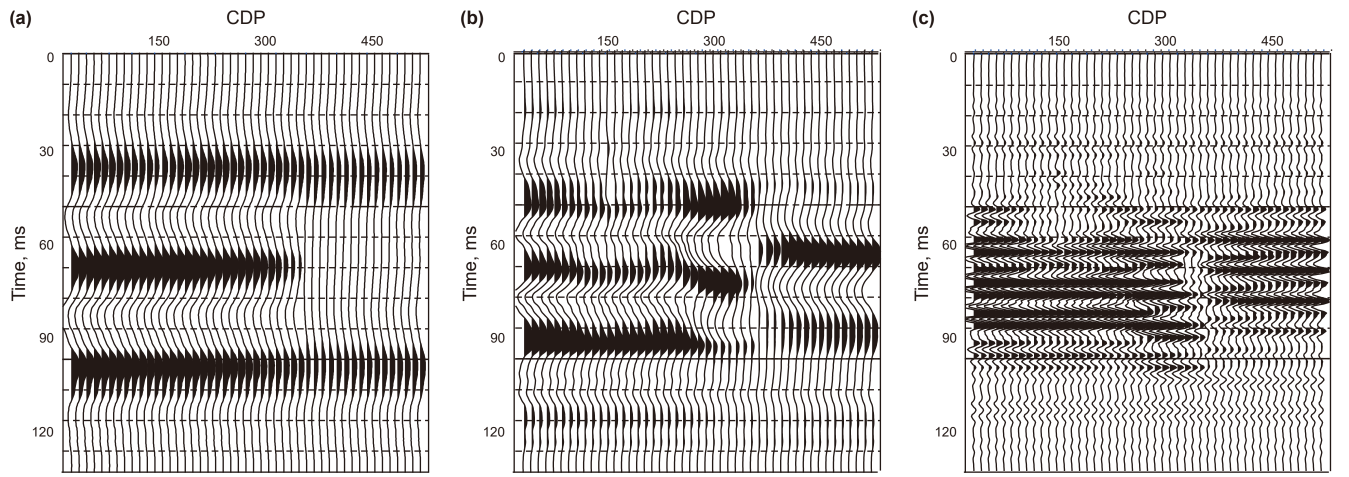

Fig. 7. The low-frequency, medium-frequency, and high-frequency information of post-stack seismic data. **(a)** Low-frequency information of seismic data. **(b)** Medium-frequency information of seismic data. **(c)** High-frequency information of seismic data.

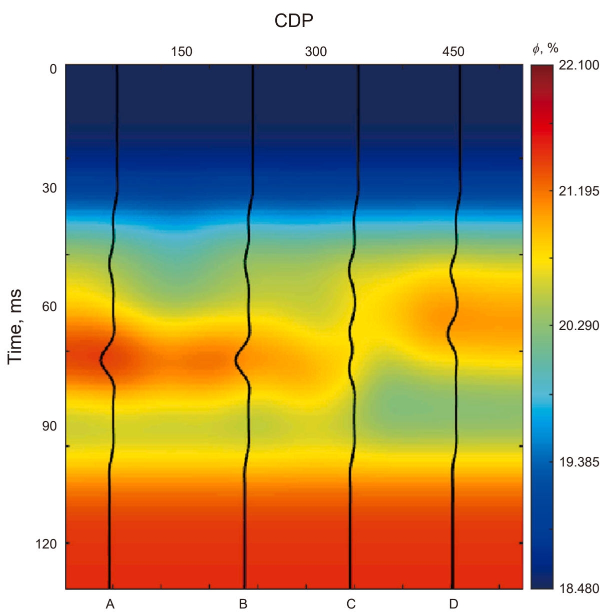

Fig. 8. The original low-frequency information of porosity.

out (red box) areas. Moreover, the WTCLPI fusion network achieves lateral continuity in its inversion results that is similar to that of the seismic data (Fig. 6), while also outperforming the traditional closed-loop neural network. This improvement can be attributed to the amplification of training samples through KDE, which effectively alleviates the problem of network training instability and over-fitting caused by insufficient samples. Moreover, the wavelet transform is used to extract the multi-scale features of seismic data, which alleviates the problem of feature ambiguity caused by mixed frequency input and enhances the ability to analyze transverse geological structure. Furthermore, to further evaluate the noise robustness of the method proposed, random noise with a signal-to-noise ratio (SNR) of 3 is added to the synthetic seismic records and then fed into the trained network model. The results show that the WTCLPI fusion network can still maintain high inversion stability and can effectively identify pinch-out and superimposed areas (Fig. 9(c)). This shows that the WTCLPI fusion network has strong anti-noise ability and generalization performance.

To facilitate a clearer comparison between different methods, the inversion results at well C are analyzed (Fig. 10), and the RMSE and R^2 indicators are used for quantitative evaluation (Table 1). Compared with the traditional closed-loop neural network, the inversion results of the WTCLPI fusion network have better

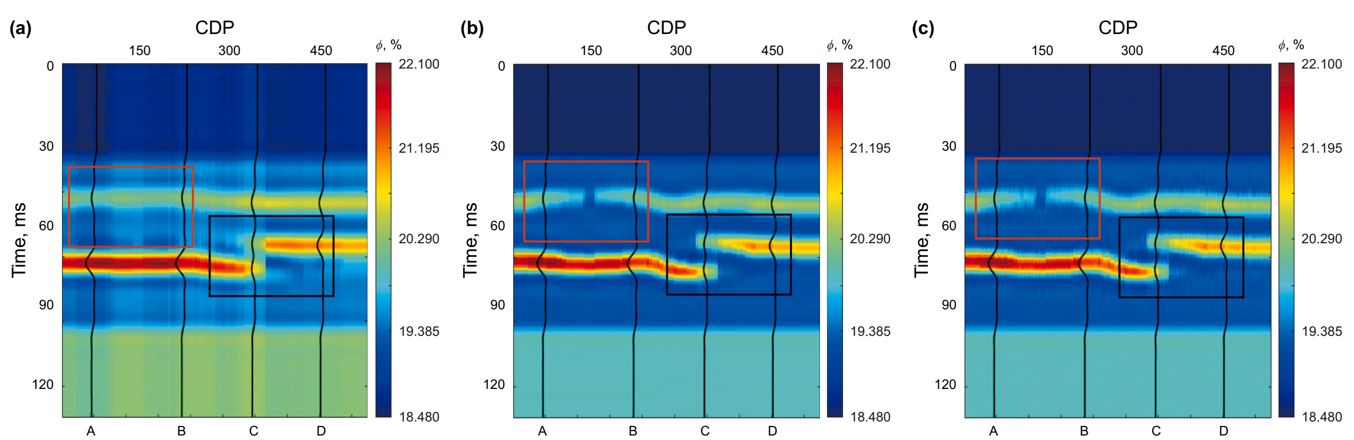

Fig. 9. The inversion results of different methods. **(a)** The inversion results of the traditional closed-loop neural network. **(b)** The inversion results of the WTCLPI fusion network without the nose. **(c)** The inversion results of the WTCLPI fusion network with the nose.

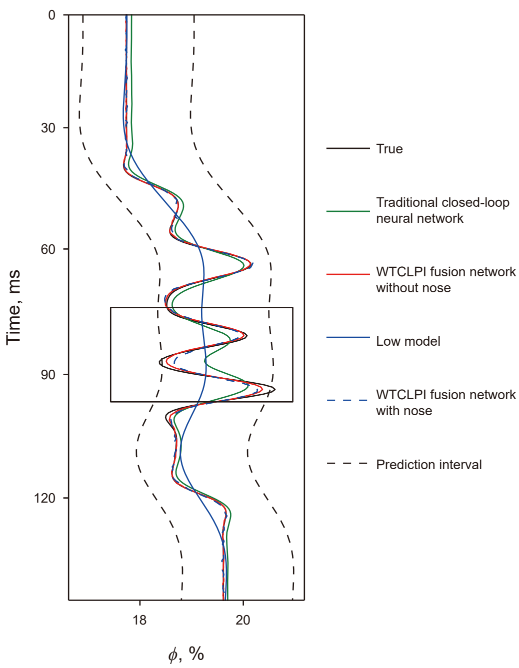

Fig. 10. Comparison of inversion results of different methods.

Table 1
Quantitative evaluation of inversion results of different methods.

Methods	R^2	RMSE
Traditional closed-loop neural network	0.893	0.253
WTCLPI fusion network with nose	0.949	0.170
WTCLPI fusion network without nose	0.952	0.164

consistency with the real values, and the superposition area (black box) is effectively identified. Moreover, the R^2 of the inversion results is 5.9% higher than that of the traditional closed-loop neural network, indicating that the method proposed has higher generalization ability. In addition, under noisy seismic data conditions, the WTCLPI fusion network still maintains higher inversion stability and accuracy. Although its R^2 decreases to some extent, the reduction remains within an acceptable range, demonstrating that the method proposed exhibits stronger robustness against noise interference.

To verify the rationality of the method proposed, three sets of experiments are designed. By controlling variables, three schemes are constructed: “high-frequency removed”, “medium-frequency removed”, and “low-frequency removed”. Under the condition that the network architecture and training strategy remained unchanged, each scheme is tested separately (Fig. 11). The inversion results show that the lack of seismic data in different frequency bands has different effects on the inversion accuracy. When high-frequency information is absent, the inversion results for shale reservoirs become blurred, and the ability to resolve fine-scale features is significantly reduced, particularly in pinch-out and superimposed areas. In the absence of medium-frequency information, the overall geological framework remains recognizable; however, the continuity and morphological accuracy of the inversion are partially degraded. When low-frequency information is absent, local details are preserved, but the background trends become unstable and lateral continuity deteriorates. These observations demonstrate that different frequency components play distinct and irreplaceable roles in the inversion process, highlighting the necessity of incorporating multi-frequency seismic information in the proposed method.

Fig. 12 shows the inversion results of the WTCLPI fusion network when different frequency bands of seismic data are removed, and the results are quantitatively evaluated using RMSE and R^2 (Table 2). Compared with the method proposed in this study, the inversion accuracy decreases by approximately 11.2%, 3.4%, and 1.7% for the “high-frequency removed”, “medium-frequency removed”, and “low-frequency removed” scenarios, respectively. These results indicate that seismic data from different frequency bands make unequal contributions to the inversion process. In particular, the absence of high-frequency information leads to a significant reduction in resolution and structural delineation. In contrast, the absence of medium- or low-frequency information results in only a slight decrease in inversion accuracy, suggesting that these components mainly contribute to overall trends and background structural continuity.

4. Actual data application

To verify the effectiveness of the method proposed, the WTCLPI fusion network is applied to the D oilfield in northwestern China, where the target layer is a shale oil reservoir at depths ranging from 2900 ms to 3100 ms. The effective pores primarily consist of microcracks, fractures, and micropores, resulting in low porosity and permeability. Fig. 13 shows the post-stack seismic profiles of the 3D data volume through wells XJ-1, XJ-2, and XJ-3, consisting

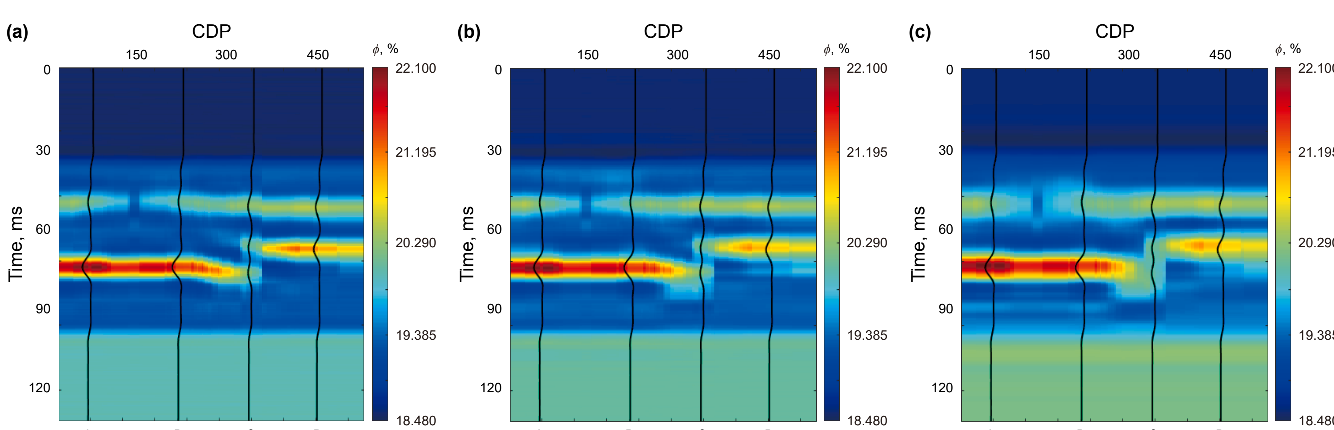

Fig. 11. The inversion results of the WTCLPI fusion network. **(a)** Low-frequency removed. **(b)** Medium-frequency removed. **(c)** High-frequency removed.

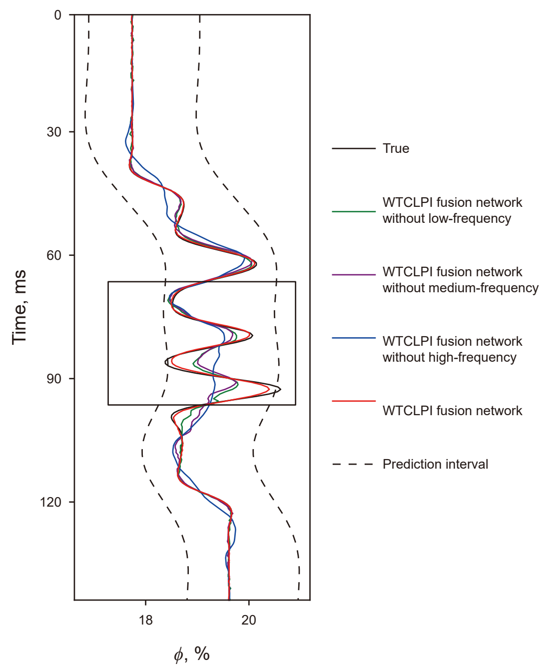

Fig. 12. Comparison of inversion results of different methods.

Table 2
Quantitative evaluation of inversion results of different methods.

Methods	R^2	RMSE
WTCLPI fusion network without low-frequency	0.935	0.173
WTCLPI fusion network without medium-frequency	0.918	0.225
WTCLPI fusion network without high-frequency	0.840	0.386

of 410 CDP traces with a dominant frequency of 30 Hz. Each seismic trace contains 50 sampling points with a sampling interval of 2 ms. The curves are natural gamma. The post-stack seismic reflection interfaces exhibit strong heterogeneity (red box), indicating significant lateral lithology changes. Fig. 14 shows the low-, medium-, and high-frequency information of post-stack seismic data obtained by wavelet transform. The frequency band ranges are 0–10 Hz, 11–30 Hz, and higher than 30 Hz, respectively. The low-frequency information mainly reflects the large-scale features, the medium-frequency information reflects the medium-scale features, and the high-frequency information reflects the detailed features. By analyzing this different frequency information, the features of the underground geological structure can be understood more comprehensively. The wells XJ-1 and XJ-3 are selected for training sample amplification, while the unlabeled post-stack seismic data are input into the network for adaptive learning to further improve the generalization ability of the network in actual work. Finally, well XJ-2 is employed as the test set to verify the effectiveness of the network.

To verify the rationality of the amplified sample, a probability histogram analysis of the amplified samples and the measured logging data is carried out, and a probability density distribution is calculated (Fig. 15). The results show that the overall distribution pattern, mean value and variance of the amplified samples are highly consistent with the measured logging data, indicating that the data generated by the amplification method can better maintain the original geological characteristics. At the same time, by superimposing the kernel density estimation curve, it can be visually observed that the amplified samples can cover the main fluctuation intervals and local extremum characteristics of the measured logging data, which further verifies the representativeness and reliability of the amplified samples in training the network.

Furthermore, to evaluate the feasibility of porosity inversion in this area and verify the sensitivity of elastic parameters to porosity (ϕ) changes, the correlation analysis between porosity and elastic parameters is carried out based on logging data (Fig. 16). By constructing the intersection diagram of porosity and compressional velocity (V_p), shear wave velocity (V_s) and density (ρ), and calculating the coefficient of determination, the response relationship between ϕ and V_p, V_s and ρ are quantitatively evaluated. The analysis results show that in the shale reservoir, porosity has a stable negative correlation with V_p, V_s, and ρ, indicating that as the ϕ increases, the overall stiffness and density of the rock skeleton decrease, resulting in a corresponding decrease in V_p and ρ. Among them, the correlation between V_p and ϕ is the most significant, reflecting that the V_p is more sensitive to the change of the bulk modulus of the rock skeleton, and can more directly capture the decrease of compressibility caused by the change of ϕ. In contrast, the correlation between V_s and ϕ is slightly weaker, indicating that the V_s is mainly controlled by the skeleton shear stiffness, while the shear stiffness is more affected by mineral composition and bedding structure in shale, thus weakening the control effect of ϕ to a certain extent. The above analysis provides a reliable physical basis for conducting porosity inversion in this area.

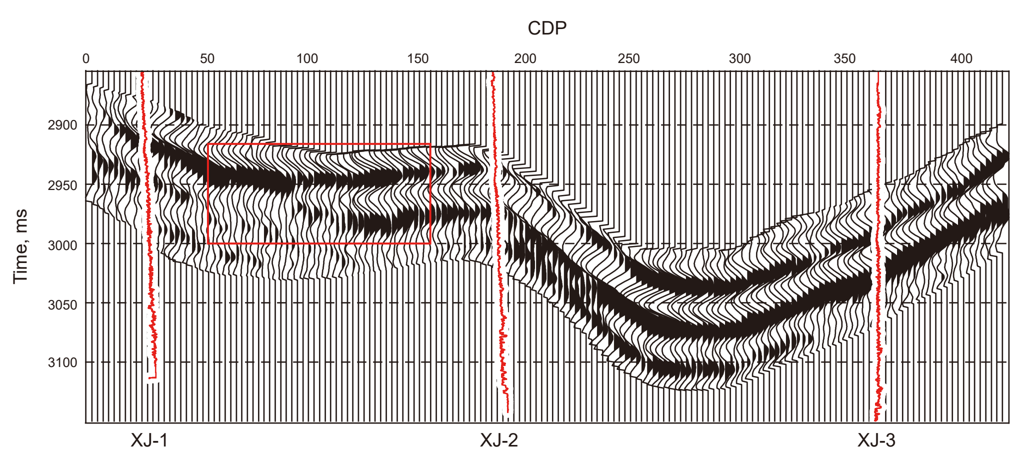

Fig. 13. The post-stack seismic data.

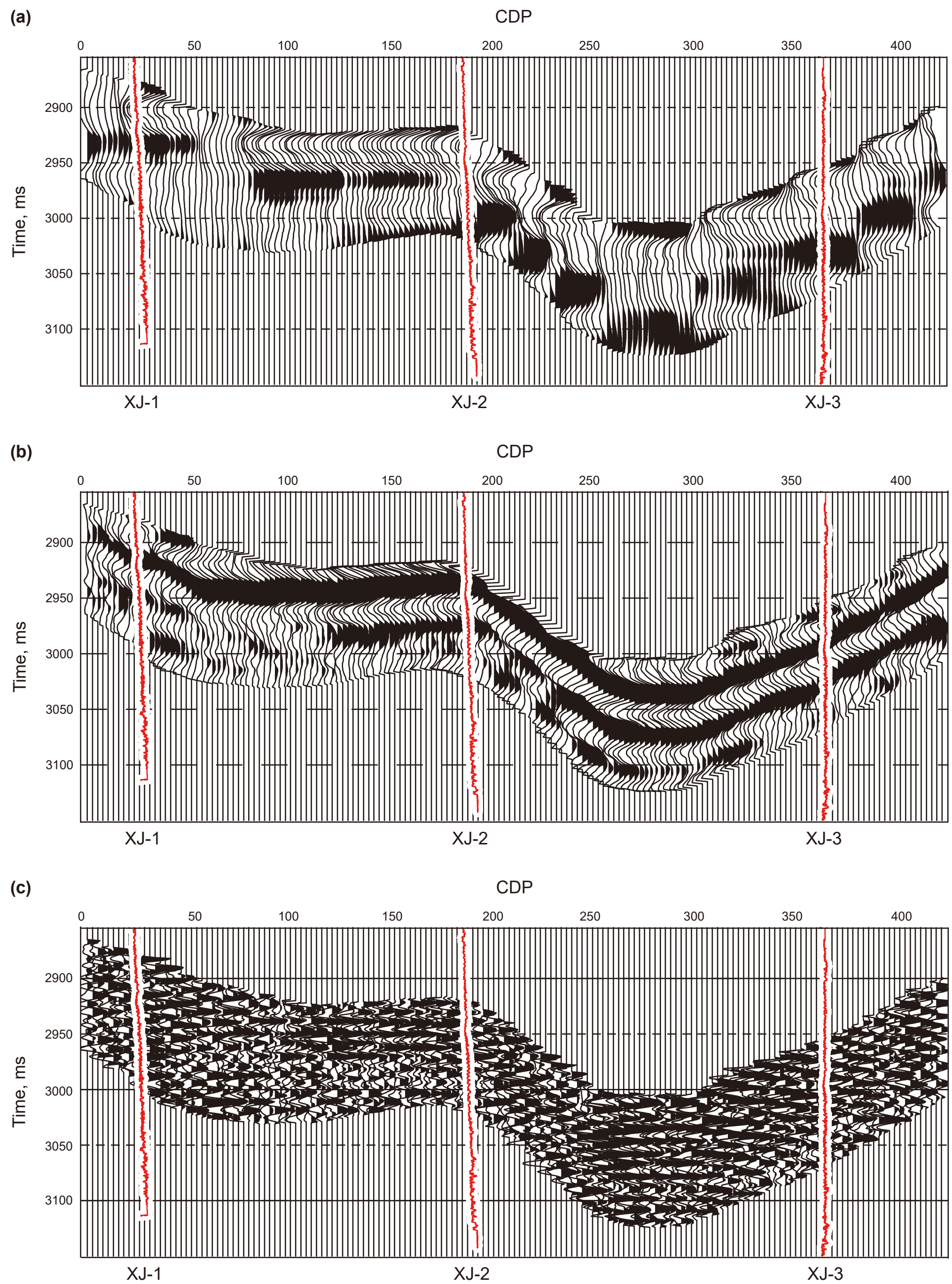

Fig. 14. The different frequency bands of post-stack seismic data. **(a)** Low-frequency information of seismic data. **(b)** Medium-frequency information of seismic data. **(c)** High-frequency information of seismic data.

Fig. 17 shows the low-frequency information of porosity. It can be observed that the values of porosity increase with the increase of depth. Since seismic data inversion is a non-unique problem, where the same seismic response can correspond to various underground features, the inversion results can be constrained by the low-frequency porosity model as prior information, thereby enhancing the stability of the neural network.

The inversion results of the traditional closed-loop neural network and the WTCLPI fusion network are compared (Figs. 18 and 19). It can be seen that the inversion results of both methods on the training set are consistent with the logging data (black box). This is because the loss of logging data supplements the high-frequency information to post-stack seismic data, overcoming its effective bandwidth limitations. However, the inversion results of the traditional closed-loop neural network exhibit insufficient lateral continuity (red box), which does not necessarily represent the real lithological variations, especially in the absence of well constraints. Under the complex geological conditions of strong lateral heterogeneity and low signal-to-noise ratio of shale oil reservoirs, the traditional closed-loop neural network is easily affected by factors such as noise amplification and inversion instability. Moreover, in the case of limited training samples, the traditional closed-loop neural network is difficult to fully learn the nonlinear mapping relationship between post-stack seismic data

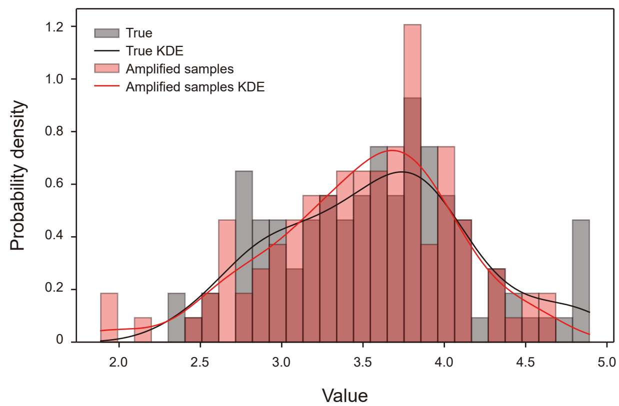

Fig. 15. Histogram and kernel density estimation comparison between the real distribution and amplified samples.

and porosity. Furthermore, directly using full-frequency post-stack seismic data as input makes it difficult for the network to effectively distinguish geological information contained in different frequency bands, due to the mixed input of low- and high-frequency components. In contrast, the KDE is used for training sample amplification to provide more data for the WTCLPI fusion network to more fully capture the distribution of geological features in the region. Subsequently, the post-stack seismic data are decomposed into low-, medium-, and high-frequency information using wavelet transform, which are combined with the full-frequency seismic data as inputs to the 3DCNN and GRU to extract spatiotemporal features from different frequency bands. This method effectively separates and utilizes the unique geological features contained in each frequency band while retaining the full-frequency seismic data, and avoids the feature interference and information aliasing that may be caused by the full-frequency input, thereby significantly enhancing the sensitivity of the network to porosity changes. Especially in the lateral direction, the complementarity between seismic responses of different frequency bands improves the recognition ability of lithological boundaries, thus improving the lateral continuity of inversion results. Furthermore, the WTCLPI fusion network replaces the forward model with neural networks, establishing a closed-loop mapping from post-stack seismic data to full-frequency porosity and back to post-stack seismic data. This not only allows for a more flexible characterization of the nonlinear relationship between seismic data and reservoir parameters but also demonstrates stronger generalization ability and stability under complex geological conditions, thereby further improving the accuracy and robustness of the inversion.

Fig. 20 shows the slices of inversion results from different methods. The results show that the inversion results of the traditional method have obvious discontinuity in the horizontal direction (black box). The inversion results of the WTCLPI fusion network show a smoother and more continuous distribution in the horizontal direction, which further verifies the advantages of the method proposed in enhancing lateral continuity. Furthermore, to verify the rationality of the above explanation, the lateral gradient evaluation index (LGE) is introduced to quantitatively evaluate the lateral variation characteristics (Table 3). The lower LGE value indicates that the random lateral gradient

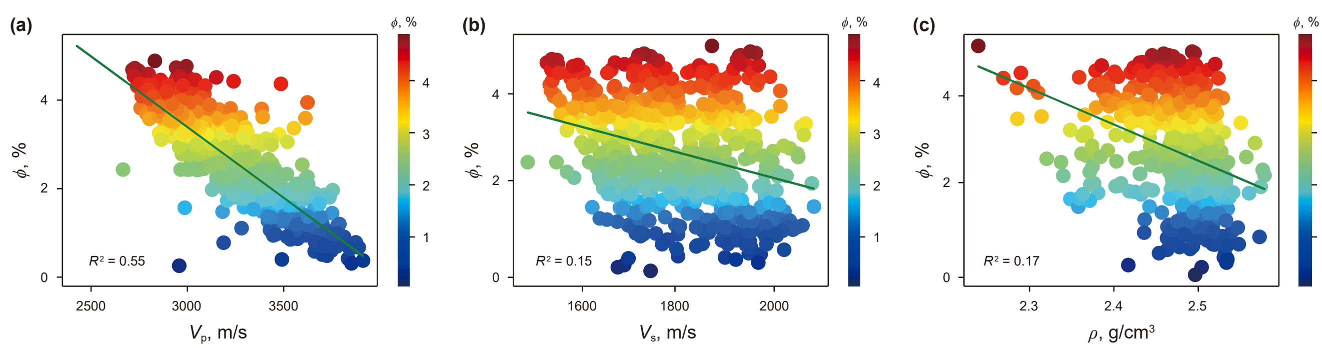

Fig. 16. The cross plot of elastic parameters and porosity. **(a)** ϕ–V_p, **(b)** ϕ–V_s, **(c)** ϕ–ρ.

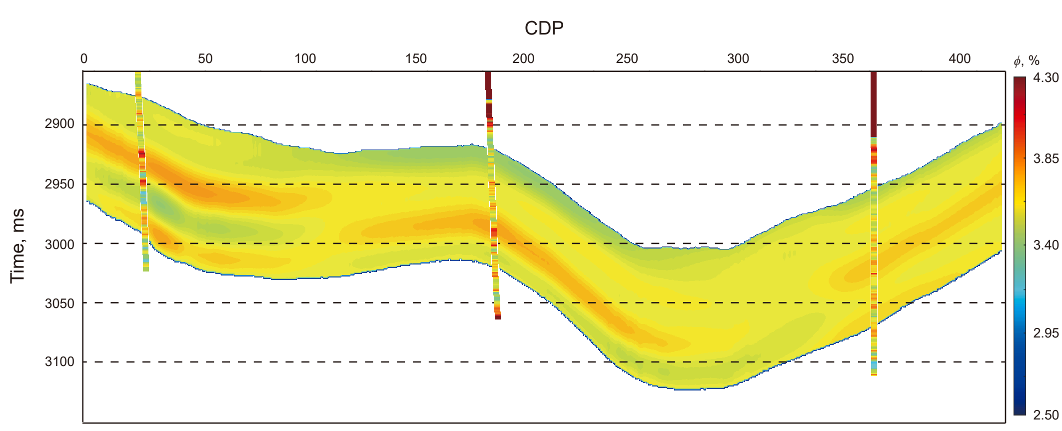

Fig. 17. The low-frequency information of porosity.

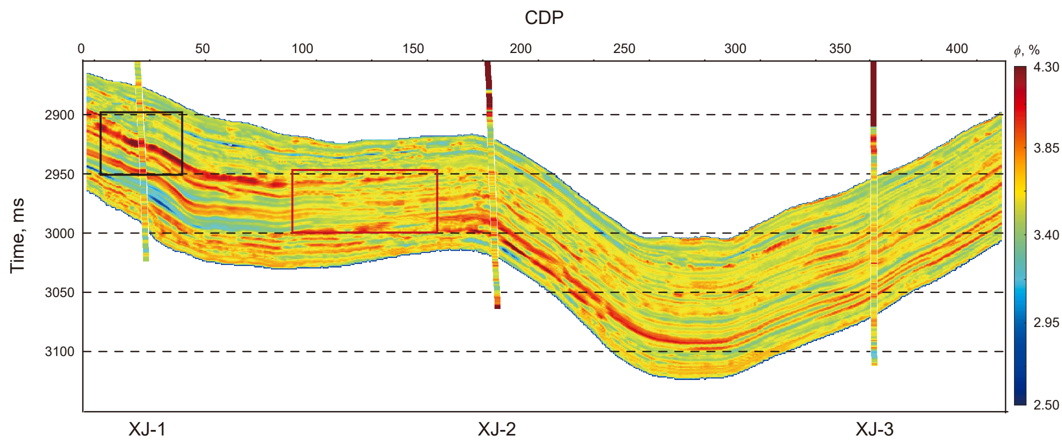

Fig. 18. The porosity results of the traditional closed-loop neural network.

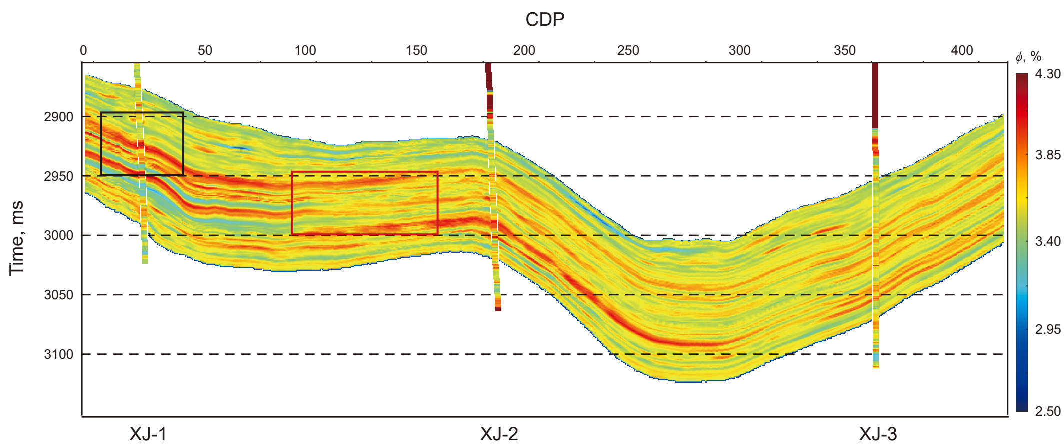

Fig. 19. The porosity results of the WTCLPI fusion network.

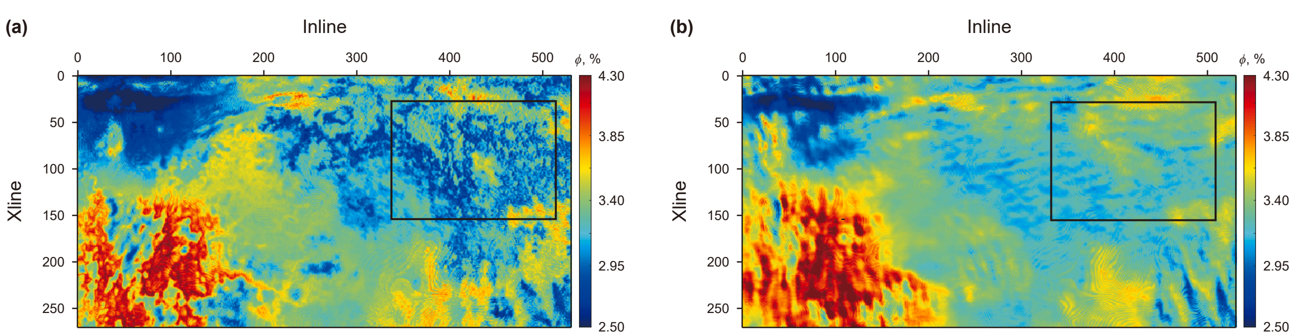

Fig. 20. The slices of inversion results from different methods. **(a)** The inversion results of the traditional closed-loop neural network. **(b)** The inversion results of the WTCLPI fusion network.

Table 3
Quantitative evaluation of the lateral resolution of inversion results by different methods.

Methods	LGE
Traditional closed-loop neural network	0.075
WTCLPI fusion network	0.044

fluctuation is weak. The experimental results show that the LGE of the WTCLPI fusion network is significantly lower than that of the traditional closed-loop neural network, indicating that the proposed method can effectively suppress noise-induced lateral discontinuities.

To further verify the effectiveness of the method proposed, the inversion results of the two methods in XJ-2 well are compared (Fig. 21), and the inversion results are quantitatively evaluated by R^2 and RMSE (Table 4). Compared with the traditional closed-loop neural network, the inversion results of the WTCLPI fusion network are closer to the true values. In addition, the R^2 of the inversion results of the WTCLPI fusion network is 11.1% higher than that of the traditional closed-loop neural network, and the

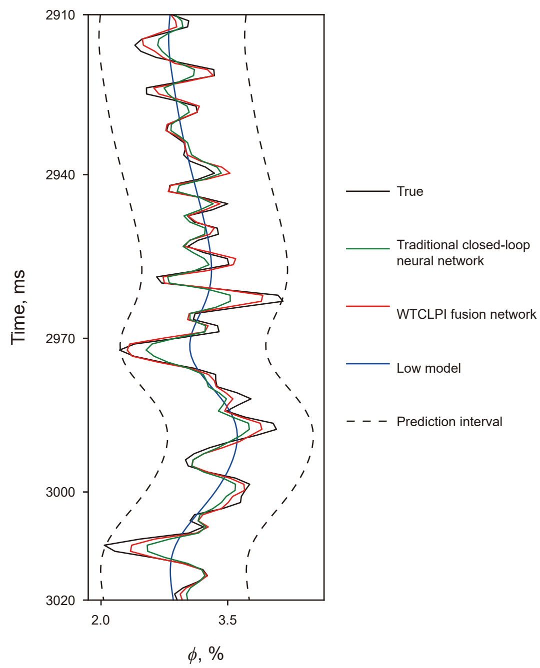

Fig. 21. Comparison of inversion results of different methods.

Table 4
Quantitative evaluation of inversion results of different methods.

Methods	R^2	RMSE
Traditional closed-loop neural network	0.808	0.435
WTCLPI fusion network	0.919	0.220

RMSE is 0.215 lower, indicating that the WTCLPI fusion network can better capture the detailed changes of porosity and the changes of thin layers.

5. Discussion

The traditional porosity inversion method is largely constrained by the effective bandwidth of seismic data and the accumulation of inversion errors, resulting in a weak ability to characterize thin layers. Building on previous research, a closed-loop porosity inversion method based on the wavelet transform is proposed. The results of this study indicate a significant improvement in the lateral continuity of the inversion profiles. The analysis of multi-frequency characteristics shows that the wavelet transform plays a key role in enhancing lateral continuity. By decomposing the seismic data into low-, medium-, and high-frequency information, the low-frequency information primarily governs regional structural trends and interlayer continuity, thereby providing a more stable background constraint within the network. Whereas high-frequency information mainly contributes to thin layers and fine details, with a relatively limited effect on overall continuity. Furthermore, the closed-loop structure enforces consistency between seismic data and porosity through the forward network, which means that the improvement of lateral continuity is also the result of physical constraints. Therefore, multi-frequency feature fusion and closed-loop consistency constraints are the main factors to improve the lateral continuity of inversion.

However, there are still some issues worth further discussion. Firstly, although kernel density estimation effectively alleviates the instability caused by insufficient training samples, the quality of the amplified samples still depends on the representativeness of the logging data distribution. When the well control is sparse or the geological changes are strong, the amplified samples based on KDE may not fully reflect the complexity of reservoir heterogeneity, thus affecting the generalization ability of the network. Secondly, although the closed-loop structure effectively establishes a nonlinear mapping relationship between seismic data and porosity, its performance is still affected by the accuracy of the forward network. Under the geological conditions with significant lithology differences or complex pore structure, there may be a deviation between the learned forward model and the real underground response, and then the error is accumulated in the closed-loop process, which affects the inversion accuracy. Therefore, the network parameters and network structure need to be finely adjusted. Thirdly, although the lateral continuity of the inversion results is significantly enhanced, the enhanced continuity may lead to the smoothing of the geological interface, and the very thin interbeds or micro-scale lateral changes may be weakened to a certain extent. Future research can combine multi-attribute resolution indicators or structural boundary comparison analysis to more comprehensively evaluate resolution changes. Finally, like most deep learning inversion methods, the method proposed in this paper still faces the risk of overfitting and insufficient cross-region generalization ability, and may not be directly applicable to other areas with different sedimentary environments, diagenesis, pore types, or acquisition parameters. Therefore, future research will focus on addressing the aforementioned issues.

6. Conclusion

Aiming at the problems of poor lateral continuity and error accumulation in traditional porosity inversion methods, a closed-loop porosity inversion method based on the wavelet transform is proposed. The training samples are amplified using kernel density estimation to alleviate the instability of neural network inversion results caused by insufficient training data. Subsequently, the post-stack seismic data are decomposed into multi-frequency information using the wavelet transform, so as to effectively capture the geological features of different scales. Meanwhile, the convolution model is replaced by a neural network to alleviate the problem of an unclear relationship between post-stack seismic data and porosity. Tests on both synthetic and real data demonstrate that the WTCLPI fusion network not only improves the vertical resolution of inversion results but also improves the lateral continuity of inversion results. In the testing sample, compared with the traditional method, the WTCLPI fusion network shows higher stability and robustness when dealing with complex reservoir structures. The R^2 of the WTCLPI fusion network increased to 91.9%, while the RMSE decreased to 0.220, which proves that the method has high prediction accuracy and generalization.

CRediT authorship contribution statement

Teng-Fei Chen: Writing – original draft. **Guang-Zhi Zhang:** Conceptualization. **Hong-Jian Hao:** Formal analysis. **De-Kuan Chang:** Supervision. **Jian-Hu Gao:** Visualization. **Gang Gao:** Methodology.

Data availability

The original accessible data has been included in the paper.

Declaration of competing interest

The authors declare that they have no known competing financial interests or personal relationships that could have appeared to influence the work reported in this paper.

Acknowledgements

This research was funded by the National Nature Science Foundation of China (Grant No. U23B6010). Thanks to Geosoftware for HampsonRussell Suite software support.

References

Abid, M., Ba, J., Markus, U.I., et al., 2025. Modified approach to estimate effective porosity using density and neutron logging data in conventional and unconventional reservoirs. J. Appl. Geophys. 233, 105571. https://doi.org/10.1016/j.jappgeo.2024.105571.

Alfarraj, M., AlRegib, G., 2019. Semisupervised sequence modeling for elastic impedance inversion. Interpretation 7 (3), SE237–SE249. https://doi.org/10.1190/INT-2018-0250.1.

Ba, J., Fang, Z.J., Fu, L.Y., et al., 2023. Seismic inversion method for tight sandstone reservoir properties based on a variable critical porosity model. Chin. J. Geophys. 66 (6), 2576–2591. https://doi.org/10.6038/cjg2022Q0106 (in Chinese).

Barros, L., Dietrich, M., Valette, B., 2010. Full waveform inversion of seismic waves reflected in a stratified porous medium. Geophys. J. Int. 182 (3), 1543–1556. https://doi.org/10.1111/j.1365-246X.2010.04696.x.

Bashir, Y., Siddiqui, N.A., Morib, D.L., et al., 2024. Cohesive approach for determining porosity and P-impedance in carbonate rocks using seismic attributes and inversion analysis. J. Pet. Explor. Prod. Technol. 14 (5), 1173–1187. https://doi.org/10.1007/s13202-024-01767-x.

Bengio, Y., Simard, P., Frasconi, P., 1994. Learning long-term dependencies with gradient descent is difficult. IEEE Trans. Neural Network. 5 (2), 157–166. https://doi.org/10.1109/72.279181.

Chen, T., Gao, G., Liu, H.J., et al., 2023. Rock brittleness index inversion method with constraints of seismic and well logs via a CNN-GRU fusion network based on the spatiotemporal attention mechanism. Geoenergy Sci. Eng. 225, 211646. https://doi.org/10.1016/j.geoen.2023.211646.

Cho, K., Van, M.B., Bahdanau, D., et al., 2014. On the properties of neural machine translation: Encoder–decoder approaches. In: Proceedings of SSST-8, eighth workshop on syntax, semantics and structure in statistical translation, pp. 103–111. https://doi.org/10.3115/v1/W14-4012.

Das, V., Pollack, A., Wollner, U., et al., 2019. Convolutional neural network for seismic impedance inversion. Geophysics 84 (6), R869–R880. https://doi.org/10.1190/geo2018-0838.1.

Duan, Y.X., Li, G.T., Sun, Q.F., 2016. Research on convolutional neural network for reservoir parameter prediction. J. Commun. 37 (S1), 1–9. https://doi.org/10.11959/j.issn.1000-436x.2016240.

Figueiredo, L.P.D., Grana, D., Bordignon, F.L., et al., 2018. Joint bayesian inversion based on rock-physics prior modeling for the estimation of spatially correlated reservoir properties. Geophysics 83 (5), M49–M61. https://doi.org/10.1190/geo2017-0463.1.

Ge, Q., Cao, H., Yang, Z.F., et al., 2022. High-resolution seismic impedance inversion integrating the closed-loop convolutional neural network and geostatistics: An application to the thin interbedded reservoir. J. Geophys. Eng. 19 (3), 550–561. https://doi.org/10.1093/jge/gxac035.

Gong, A., Zhang, H., 2024. Reservoir fluid identification model based on wavelet transform and CNN-transformer. Journal of Xi'an Shiyou University (Natural Science Edition) 39 (4), 108–116. https://doi.org/10.3969/j.issn.1673-064X.2024.04.015 (in Chinese).

Han, H.H., Liu, H.J., Sang, W.J., et al., 2022. Seismic and well logs integration for reservoir lateral porosity prediction based on semi supervised learning. Chin. J. Geophys. 65 (10), 4073–4086. https://doi.org/10.6038/cjg2022P0410 (in Chinese).

He, R.F., Ba, J., Chen, T.X., et al., 2020. Study on fracture-pore elastic rock physics template of tight sandstone gas reservoirs: A case study of area A in West Sichuan depression. Prog. Geophys. 35 (1), 116–123. https://doi.org/10.6038/pg2020DD0040 (in Chinese).

Kamalov, F., Elnagar, A., 2021. Kernel density estimation-based sampling for neural network classification. arXiv:2110.12644. doi: 10.48550/arXiv.2110.12644.

Kamel, M.H., Mabrouk, W.M., Bayoumi, A.I., 2002. Porosity estimation using a combination of Wyllie–Clemenceau equations in clean sand formation from acoustic logs. J. Petrol. Sci. Eng. 33 (4), 241–251. https://doi.org/10.1016/S0920-4105(01)00169-3.

Khaksar, A., Griffiths, C., 1998. Porosity form sonic log in gas-bearing shaly sandstones: Field data versus empirical equations. Explor. Geophys. 29 (4), 440–446. https://doi.org/10.1071/EG998440.

Liu, J.S., Sun, Y.H., Liu, Y., 2022. Model-data-driven seismic inversion method based on small sample data. Petrol. Explor. Dev. 49 (5), 1046–1055. https://doi.org/10.11698/PED.20220119 (in Chinese).

Liu, K.Y., He, Z.H., Xu, Y.Q., 2014. Porosity prediction method research for carbonate reservoir and its application in South China Sea. Geophys. Prospect. Pet. 53 (2), 232–237. https://doi.org/10.3969/j.issn.1000-1441.2014.02.014 (in Chinese).

Miraj, M.R., Huang, H., Yang, T., et al., 2025. GK-SMOTE: A hyperparameter-free noise-resilient Gaussian KDE-based oversampling approach. https://doi.org/10.48550/arXiv.2509.11163.

Mukun, Y., Jian, L., Chen, Z.Y., et al., 2024. Virtual sample generation for industrial soft-sensing models in sparse data environments: A data augmentation approach using UMAP-KDE. Comput. Chem. Eng. 193, 108925. https://doi.org/10.2139/ssrn.5050714.

Pan, X., Li, X.Y., Huang, L., et al., 2024. Estimation of fracture properties from azimuthal seismic data using convolution neural network. IEEE Geoscience and Remote Sensing Letters 21, 3002005. https://doi.org/10.1109/LGRS.2024.3387699.

Pan, X., Zhang, Z., Yin, X., 2018. Probabilistic seismic inversion for reservoir fracture and petrophysical parameters driven by rock-physics models. Chin. J. Geophys. 61 (2), 683–696. https://doi.org/10.6038/cjg2018K0759 (in Chinese).

Pan, X., Zhang, Z., Zhang, J., et al., 2017. Zoeppritz-based AVO inversion using an improved markov chain monte carlo method. Pet. Sci. 14 (1), 75–83. https://doi.org/10.1007/s12182-016-0131-4.

Sang, W.J., Yuan, S.Y., Ding, Z.Q., et al., 2024. Data-model jointly driven acoustic impedance inversion. Chin. J. Geophys. 67 (2), 696–710. https://doi.org/10.6038/cjg2023R0147 (in Chinese).

Sun, Y.H., Liu, Y., 2020. Prediction of S-wave velocity based on GRU neural network. Oil Geophys. Prospect. 55 (3), 484–492. https://doi.org/10.13810/j.cnki.issn.1000-7210.2020.03.001 (in Chinese).

Tong, J.N., Sun, X.W., Wang, F., et al., 2025. Intelligent facies-controlled seismic meme inversion and its application in predicting thin reservoirs in coal measure strata. Geophys. Prospect. Pet. 64 (1), 129–137. doi: CNKI: SUN: SYWT.0.2025-01-010 (in Chinese).

Wang, B., Niu, C., Li, Y., et al., 2019. Application of frequency division inversion based on generalized S transform in oil and gas exploration in deep water area of South China Sea. Prog. Geophys. 34 (6), 2508–2514. https://doi.org/10.6038/pg2019CC0439 (in Chinese).

Wang, T.T., Wang, Z.H., Zhao, W.C., et al., 2025. Intelligent lithology identification based on MSCNN-GRU neural network to complement logging curves and interpretability. Oil Geophys. Prospect. 60 (1), 1–11. https://doi.org/10.13810/j.cnki.issn.1000-7210.20240144 (in Chinese).

Wang, W.R., Yue, D.L., Li, W., et al., 2024. Prediction of single-layer sand body by spectral-decomposition intelligent inversion collaborating 3D lithofacies modeling. Chin. J. Geol. 59 (6), 1694–1707. https://doi.org/10.12017/dzkx.2024.116 (in Chinese).

Wang, Y.Q., Ge, Q., Lu, W.K., et al., 2020. Well-logging constrained seismic inversion based on closed-loop convolutional neural network. IEEE Trans. Geosci. Rem. Sens. 58 (8), 5564–5574. https://doi.org/10.1109/TGRS.2020.2967344.

Wyllie, M.R.J., Gregory, A.R., Gardner, L.W., 1956. Elastic wave velocities in heterogeneous and porous media. Geophysics 21 (1), 41–70. https://doi.org/10.1190/1.1438217.

Xu, S., Payne, M.A., 2009. Modeling elastic properties in carbonate rocks. Lead. Edge 28 (1), 66–74. https://doi.org/10.1190/1.3064148.

Yang, F., Liu, Y., Chang, S., et al., 2024. Prestack seismic porosity prediction method based on bidirectional GRU and attention mechanism. Geophys. Prospect. Pet. 63 (3), 598–609. https://doi.org/10.12431/issn.1000-1441.2024.63.03.008 (in Chinese).

Zhai, X.Y., Gao, G., Liu, H.J., et al., 2024. Research on elastic parameter inversion method based on seismic facies-controlled deep learning network. Comput. Geosci. 193, 105739. https://doi.org/10.1016/j.cageo.2024.105739.

Zhang, B., Mi, H., Liu, H., et al., 2025. Pre-stack seismic inversion method for physical properties of complex tight sandstone reservoirs based on the rock physics model. Prog. Geophys. 40 (1), 220–229. https://doi.org/10.6038/pg2025HH0583 (in Chinese).

Zhang, C.F., Ni, S.D., Zhang, H., et al., 2025. The denoising method for high-rate GNSS seismic waves combining auto-encoder neural networks and wavelet transform. Chin. J. Geophys. 68 (1), 66–80. https://doi.org/10.6038/cjg2024R0877 (in Chinese).

Zhang, G.D., Zhang, H.B., Zhao, J.Q., et al., 2025. Evaluating CNN-based models for seismic data denoising. Geophys. Prospect. Pet. 64 (2), 232–246. https://doi.org/10.12431/issn.1000-1441.2023.0365 (in Chinese).

Zhang, H.H., Zhang, G.Z., Gao, J.H., et al., 2022. Seismic impedance inversion based on geophysical-guided cycle-consistent generative adversarial networks. J. Petrol. Sci. Eng. 218, 111003. https://doi.org/10.1016/j.petrol.2022.111003.

Zhang, S.Z., Zhang, Z., Zhou, Y., et al., 2022. Estimation of fracture porosity using ES-DBN network based on seismic multiple attributes. Prog. Geophys. 37 (6), 2492–2497. https://doi.org/10.6038/pg2022FF0364 (in Chinese).

Zhang, Y.M., Qin, X.Y., Guo, Z.Q., et al., 2021. Petrophysical model for complex pore structure and its applications in tight sand gas reservoirs. J. Jilin Univ. (Earth Sci. Ed.) 51 (3), 927–929. https://doi.org/10.13278/j.cnki.jjuese.20200277 (in Chinese).